Bull. Nov. Comp. Center, Num. Model. in Atmosph., etc., 5 (1999), 11–26

The use of satellite remote sensing data in numerical modeling of the North Pacific circulation*

V. Kuzin, V. Moiseev, A. Martynov

A numerical model constructed in the Institute of Computational Mathematics and Mathematical Geophysics (the former Novosibirsk Computing Center), based on the finite element method has been used for investigation of the sensitivity of the Pacific ocean circulation to a climatic (Hellerman and Rosenstein [1]) and satellite derived (Halpern et al. [2]) wind forcing. The model grid covers the region between 30 S and 60 N with space resolution 2° in longitude and 1° in latitude, with 18 levels in depth. The model includes a block of vertical mixture in the upper layer [3].

Diagnostic experiments have been carried out for April and October, 1994. We have selected these two months for modeling different ocean circulation states with weak wind in April (switch from winter monsoon to summer monsoon) and strong wind in October (switch from summer monsoon to winter monsoon). Also, the short-range prognostic experiments for both climatic and satellite data were carried out for the 3-year period with a seasonal cycle.

Analysis of the obtained results has shown that the general circulation of the Pacific ocean did not essentially change depending on different data used. Nevertheless, a more complicated current structure has been obtained with the use of satellite data. At the same time, the main boundary currents are more intensive, and the volume transport estimates have shown higher values when climatological data applied.

1. Introduction

In order to describe and to understand the interannual variability of the ocean circulation processes with the use of numerical models, the attention has to be attracted to the quality of various sources of the surface wind as one of important forcing parameters as well as to the sensitivity of the model to the variation of this forcing. A comparison of different surface wind stress products shows that application of the modern satellite data may correct or improve climatologies traditionally used by modelers, and may produce a more realistic ocean circulation [4, 5].

There are several surface wind products which may be used to force the ocean circulation models:

*Supported by the Russian Foundation for Basic Research under Grant 99–05–64684.

- Hellerman–Rosenstein climatology [1];
- Comprehensive Ocean-Atmosphere Data Set (COADS);
- European Centre for Medium-Range Weather Forecast (ECMWF);
- Goddard Earth Observing System (GEOS);
- An atlas of monthly mean distribution of SSMI surface wind speed, AVHRR/2 sea surface temperature, AMI surface wind velocity, and TOPEX/POSEIDON sea surface height during 1987–1997, etc.

In this paper, the Novosibirsk Computing Center Finite Element Ocean Circulation Model (FEOCM) was applied for the comparison of two sources:

- monthly averaged wind stress data of Hellerman and Rosenstein [1] and
- monthly mean AMI surface wind speed, Halpern et al. [2].

In the previous works, this model was used for the reconstruction of the 3D velocity fields in the North Pacific employing the climatic data [6–8]. In the present study, the first stage of numerical experiments includes the diagnostic calculations for two months (April and October, 1994) with the climatic and satellite wind stress. At the next stage of the study, the short-range prognostic experiments which consist of the seasonal spin-up of the model with climatic forcing for a 3-year period and then, the 2.5-year calculation of seasonal cycles with satellite derived wind forcing were carried out.

2. Ocean circulation model

The system of equations for calculation of the 3-D fields of velocity, temperature and salinity can be written down in the form:

$$\frac{dU}{dt} + (f - \delta)\vec{k} \times U = -\frac{1}{\rho_0}\nabla P + \frac{\partial}{\partial z} v \frac{\partial U}{\partial z} + \vec{F}, \tag{1}$$

$$\mathrm{div} U + \frac{\partial w}{\partial z} = 0, \qquad \frac{\partial P}{\partial z} = g\rho, \qquad \rho = \rho(T, S), \tag{2}$$

$$\frac{d(T,S)}{dt} = \frac{\partial}{\partial z}\kappa\frac{\partial(T,S)}{\partial z} + \nabla\mu\nabla(T,S). \tag{3}$$

Equations (1)–(3) are written in the coordinates (λ, θ, z) on the sphere of radius a, where λ is longitude, $\theta = \varphi + \pi/2$, φ is latitude, z is the vertical coordinate with the positive direction from the surface toward the center of the Earth, $U = (u, v)$ is the vector of horizontal velocity components, w is the vertical velocity component, $m = 1/a\sin\theta$, $n = 1/a$, $a = 6.38 \times 10^8$ cm,

$f = -2\omega\cos\theta$ is the Coriolis parameter, $\omega = 0.73\times10^{-4}$ is the angular speed of the Earth's rotation, $\rho_0 = \text{const}$ is the standard density, ρ is density, P is pressure, ν and κ are the vertical eddy viscosity and diffusivity coefficients, respectively, μ is the horizontal diffusivity coefficient, ∇ is the spherical horizontal gradient operator, T is temperature (°C), S is salinity (‰), $\vec{k}$ is a unit vector along z–direction, $\delta = m\cos\theta u$,

$$\frac{d\varphi}{dt} = \frac{\partial\varphi}{\partial t} + mu\frac{\partial\varphi}{\partial\lambda} + nv\frac{\partial\varphi}{\partial\theta} + \frac{\partial\varphi}{\partial z} \tag{4}$$

$$\nabla P = \left(m\frac{\partial P}{\partial\lambda}, n\frac{\partial P}{\partial\theta}\right), \qquad \operatorname{div} U = m\left(\frac{\partial u}{\partial\lambda} + \frac{\partial}{\partial\theta}\frac{n}{m}v\right), \tag{5}$$

$$F = A_l\left(m\Delta U + (n^2 - m^2\cos^2\theta)U - 2m^2\cos\theta\cdot\vec{k}\times\frac{\partial U}{\partial\lambda}\right), \tag{6}$$

where A_l is the horizontal eddy viscosity coefficient,

$$\Delta\varphi = \frac{\partial}{\partial\lambda}m\frac{\partial\varphi}{\partial\lambda} + \frac{\partial}{\partial\theta}\frac{n^2}{m}\frac{\partial\varphi}{\partial\theta}, \quad \frac{d\varphi}{dt} = \frac{\partial\varphi}{\partial t} + mu\frac{\partial\varphi}{\partial\lambda} + nv\frac{\partial\varphi}{\partial\theta} + w\frac{\partial\varphi}{\partial z}. \tag{7}$$

The boundary conditions for (1)–(3) are as follows:

- at the surface:

$$z = 0: \quad w = 0, \quad \nu\frac{\partial U}{\partial z} = -\frac{\vec{\tau}}{\rho_0}, \quad (T,S) = (T^0,S^0); \tag{8}$$

- at the bottom:

$$z = H(\lambda,\theta): \quad w = U\cdot\nabla H, \quad \nu\frac{\partial U}{\partial z} = -R\overline{U},$$
$$\overline{U} = \frac{1}{H}\int_0^H U\,dz, \quad \frac{\partial(T,S)}{\partial z} = 0; \tag{9}$$

- at the cylindrical lateral boundaries $\Gamma = \Gamma_0\cup\Gamma_1$:
  a) "solid" boundary:

$$\Gamma_0: \quad \frac{\partial U\cdot\vec{l}}{\partial n} = 0, \quad \vec{U}\cdot\vec{n} = 0, \quad \frac{\partial(T,S)}{\partial n} = 0; \tag{10}$$

  b) "liquid" boundary:

$$\Gamma_1: \quad U = U^0, \quad (T,S) = (T^0,S^0). \tag{11}$$

In relations (8)–(11), $\vec{\tau}$ is a wind-stress vector, R is a bottom drag coefficient, $\vec{l}$, $\vec{n}$ are tangent and normal unit vectors to the lateral boundary Γ, respectively. The index $(^0)$ marks the values that are specified. At the

initial time values, u^0, v^0, T^0, S^0 are prescribed. The system of equations (1)–(3) is solved by the finite element technique on the staggered E-grid [9]. Equation (3) is solved by splitting [10] along the directions λ_1, θ_1, where $(\widehat{\lambda, \lambda_1}) = (\widehat{\theta, \theta_1}) = \pi/4$.

The principal features of the model realization are as follows:

- separation of the external and the internal modes;
- transformation of advective terms from the gradient form to some special divergent form;
- splitting of equations with respect to the physical processes;
- finite element method (FEM) discretization with respect to space;
- splitting of the multi-point FEM grid operators to a series of three-point operators;
- using implicit and semi-implicit schemes with respect to time.

3. Data sources and analysis

In the present study, we use the climatological monthly mean temperature and salinity fields of the "World Ocean Atlas 1994" [11] (further in the text climatological or the Levitus data), the climatological monthly mean wind stress by Hellerman–Rosenstein [1] (further in the text climatological or the Hellerman data) and satellite derived data from "Atlas of monthly mean distribution of SSMI surface wind speed, AVHRR/2 sea surface temperature, AMI surface wind velocity, and TOPEX/POSEIDON sea surface height during 1994" Halpern et al. [2] (further in the text satellite or the Halpern data). The satellite data were obtained from the FTP site ftp://poddac.jpl.nasa.gov/pub.

To estimate the opportunity of using the satellite data in numerical modeling of the general circulation of the Pacific ocean, the wind satellite data for April and October, 1994, from Halpern were selected for the diagnostic experiment. A weaker wind distribution is typical in April (switch from the winter monsoon to the summer monsoon) and a stronger wind is observed in October (switch from the summer monsoon to the winter monsoon).

The short-range prognostic calculations were successively done for the 5.5-year period with a seasonal cycle using the Hellerman and the Halpern wind products to force the model. The seasonal average of the satellite data was done using the analogous approach which was applied by S. Levitus in his Atlas [11]: Winter (February, March, April); Spring (May, June, July); Summer (August, September, October); and Autumn (November, December, January).

The following recalculation of the wind stress has been made using the ERS-1 wind vectors on the basis of the method presented in [1]:

$$\tau^x = \rho C_D u(u^2+v^2)^{1/2}, \qquad \tau^y = \rho C_D v(u^2+v^2)^{1/2},$$

$$C_D = 0.934\cdot10^{-3} + 0.788\cdot10^{-4}\,M + 0.868\cdot10^{-4}\,\Delta T - 0.616\cdot10^{-6}\,M^2 - 0.120\cdot10^{-5}(\Delta T)^2 - 0.214\cdot10^{-5}\,M\Delta T.$$

where $M = (u^2+v^2)^{1/2}$, $\Delta T = T_a - T_s$, u and v are the components of the ERS-1 surface wind vectors in cm/s, T_a is the air temperature near the sea surface, and T_s is the sea surface temperature. As we had no data for T_a, it was assumed to be equal to T_s.

The climatological subsurface temperature and salinity data were used as initial for all the experiments. Both climatological and satellite data have been applied on the surface in different simulations.

A comparison of climatological data with the satellite derived data shows the following:

Wind-stress data. The study of the wind-stress data has shown an essential structural difference as well as a difference in the maximum and the mean values: a significant difference in the whole general wind field has been observed north of 30° N and south of Japan in April (Figures 1a and 1b): for the maximum: 0.164 N (Hellerman) and 0.103 N (Halpern); for the mean values: 0.062 N (Hellerman) and 0.041 N (Halpern).

The satellite wind-stress data were rather different from the climatological data in the region sea of the Kuril Islands and sea of Kamchatka

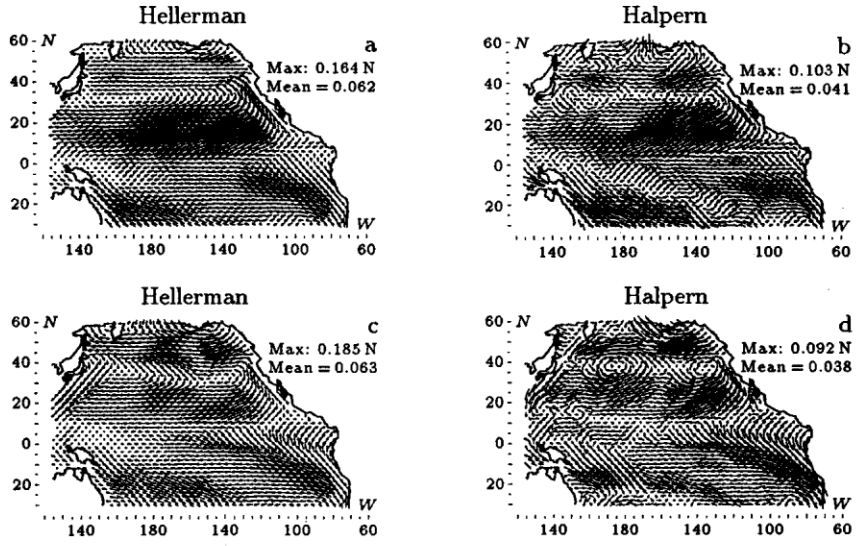

Figure 1. The monthly mean wind stress distributions in N for April (upper figures) and October (lower figures) according to *Hellerman and Rosenstein* and *Halpern*

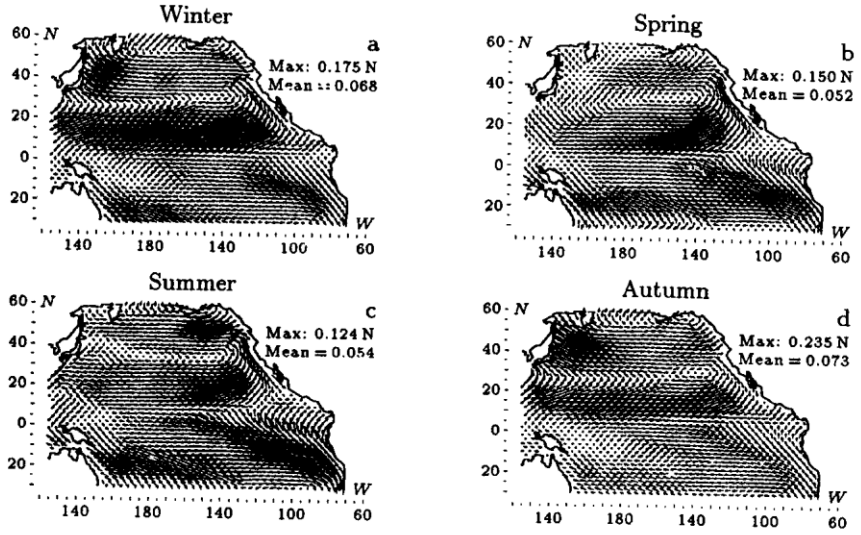

Figure 2. The climatological seasonal wind stress distributions according to *Hellerman and Rosenstein*

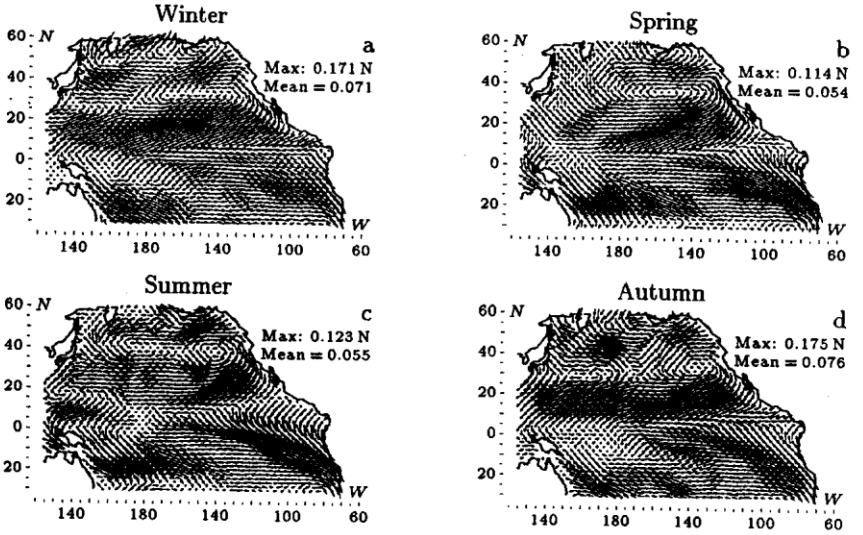

Figure 3. The satellite seasonal wind stress distributions according to *Halpern*

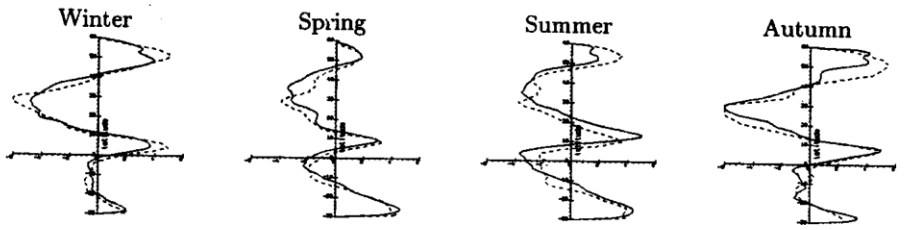

Figure 4. Seasonal zonally averaged curl distribution derived from the *Hellerman and Rosenstein* climatology (the dashed line), and from *Halpern* (solid line)

peninsula in October. Two large cyclones with the centers at about 37° N, 175° E and 35° N, 135° W have been also observed in these data (Figures 1c and 1d): for the maximum: 0.185 N (Hellerman) and 0.092 N (Halpern); for the mean values: 0.063 N (Hellerman) and 0.038 N (Halpern).

It should be noted that climatological wind-stress data have usually higher values in comparison with satellite data. At the same time, the satellite derived data are more complicated and have finer structural features.

The seasonal wind-stress fields were calculated for the prognostic experiments with the use of both climatological (Figure 2) and satellite derived data (Figure 3). These fields are rather different in structure. As a rule, they are more spatially smoothed for climatological distributions. Both stresses are more intensive during *winter* and *autumn*, and weaker during *spring* and *summer*.

The discrepancy between the climatological and the satellite derived data is shown in the seasonal zonally averaged curl distribution in Figure 4. The satellite zonally averaged curl is weaker for all the seasons except for spring in high latitudes (50–60° N). It is comparable with climatology for *spring*, *summer* and *autumn* in the westerlies. The summer curl is stronger in tropics, whereas the winter one is weaker. There is a fluctuation in the tropical extremum position relative to the equator. It shifts northward from winter to summer. The same feature is observed with the other extremum located southward the previous one in the curve. It is better developed in *summer* with the location north of the equator. Both satellite and climatological curls show similarity south of the equator where the curl maximum is observed in *spring*.

4. Numerical experiments

To test the satellite data and to make a comparison of the results obtained with the climatological data and the satellite data, the following experiments were carried out:

Ia diagnostic experiment with climatological data for April;

Ib the same with satellite data for April, 1994;

IIa diagnostic experiment with climatological data for October;

IIb the same with satellite data for October, 1994;

IIIa short-range prognostic experiment with climatological data (3 years);

IIIb short-range prognostic experiment with satellite data for the seasonal cycle of 1994 (2.5 years).

The diffusivity and viscosity coefficients in the experiments are as follows: the horizontal viscosity $A_l = 2 \times 10^6$ cm^2/s; the vertical viscosity $\nu = 10$ cm^2/s; the horizontal diffusivity $\mu = 2 \times 10^6$ cm^2/s; the vertical diffusivity $\kappa = 1$ cm^2/s. The bottom drag coefficient is $R = 10^{-7}$s^{-1}.

Experiments Ia and Ib. All the diagnostic experiments started with the state of rest and were calculated for the period of 60 days. According to the kinetic energy distribution, the solution attained the equilibrium state both in the whole domain and in the selected regions by that moment.

The simulated current fields for April and October both for climatological and satellite wind forcing are shown in Figure 5. We have deleted the southern part of the model domain in these figures because the diagnostic calculations do not adequately reproduce the circulation in the vicinity of the equator.

The simulated currents in Figures 5a and 5b have reproduced all the main currents of the North Pacific circulation. The Kuroshio and the Oyashio are compacter in the Experiment Ib with the satellite data, as well as the West Wind Drift. Two anticyclonic eddies to the right side of the Kuroshio stream correspond to a well-developed wind vorticity south of Japan in Figure 5b. Such eddies are observed in about the same positions in the observation. The Alaska current and the California current seem to be stronger and are better recognized in the Experiment Ia with climatological data. It is well known that the eastern boundary currents are tightly connected with the dominant winds in this region.

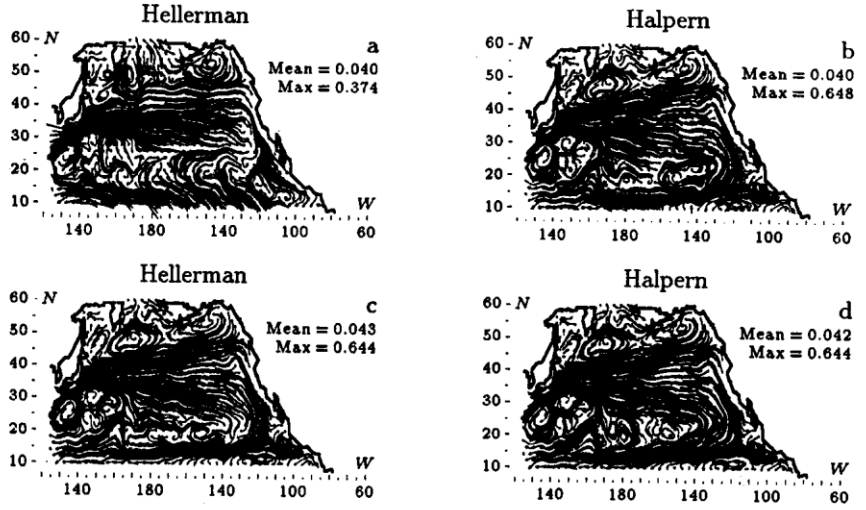

Figure 5. The simulated current velocities at the depth $Z = 50$ m for April (upper figures) and October (lower figures) according to *Hellerman and Rosenstein* and *Halpern*

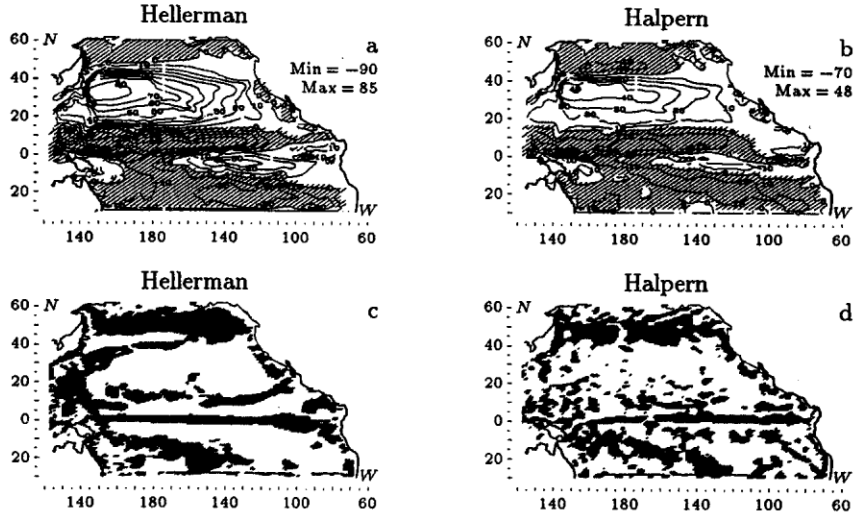

Figure 6. The simulated integral streamfunction in Sv, 1 Sv = 10^6 m^3s^{-1} (upper figures) and W-component at the depth $Z = 50$ m (lower figures, zones of upwelling are shaded) for April according to *Hellerman and Rosenstein* and *Halpern*

The stream function distribution (Figures 6a and 6b) shows a general similarity, although a subpolar gyre is much better developed in Experiment Ia, and the difference in the maximum values of the integrated mass transport is fairly large: Max = 85 Sv (Hellerman) and 48 Sv (Halpern); Min = −90 Sv (Hellerman) and −70 Sv (Halpern).

These differences in maxima have been caused by a more intensive wind-stress field in the climatological data.

Figures 6c and 6d show the distribution of the vertical velocity sign at a depth of 50 m. A solid region of upwelling is observed along the western coast of the North America; it is better developed in Experiment Ia in comparison with Experiment Ib. However, in the north-eastern part of the Pacific ocean and south of Japan (nearby the Idzu-Ogasavara Ridge) the region covered with upwelling is bigger in Experiment Ib. All these features are derived by the wind structure above the North Pacific.

Experiments IIa and IIb. Figures 5c and 5d show the horizontal velocity field at the level of 50 m. Differences in results obtained with the climatological and the satellite data are less than in Experiments Ia and Ib.

Figures 7a and 7b for the stream function show the same tendency as in Experiments Ia and Ib with the maximum values of volume transport: Max = 78 Sv (Hellerman) and 48 Sv (Halpern); Min = −50 Sv (Hellerman) and −50 Sv (Halpern).

The structure of the integral circulation in the medium and high latitudes for different kinds of data has been changed only unessentially. Implemen-

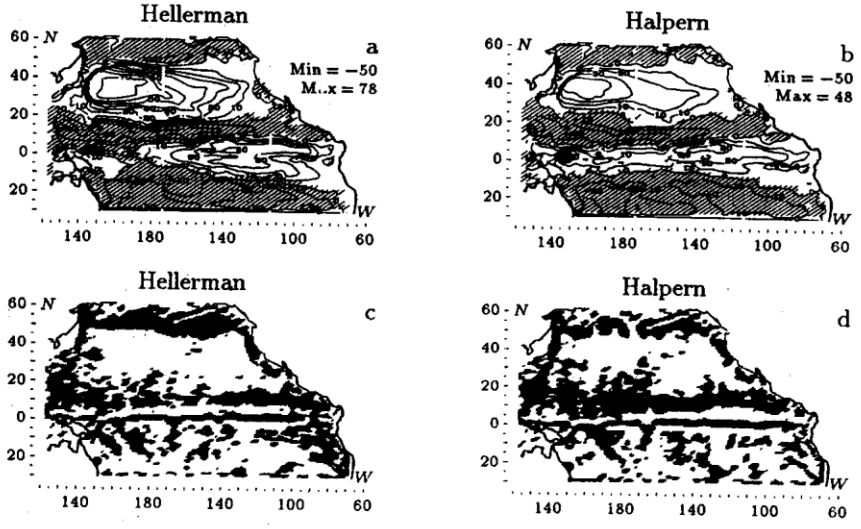

Figure 7. The simulated integral streamfunction (upper figures) and W-component at the depth $Z = 50$ m (lower figures, zones of upwelling are shaded) for October according to *Hellerman and Rosenstein* and *Halpern*

tation of the satellite data has led to a less regular circulation nearby the equator.

It should be noted, nevertheless, that the obtained results for October have shown the vaster regions covered with upwelling (Figures 7c and 7d) in the subtropical region in comparison with similar results for April (for both kinds of data).

Experiments IIIa and IIIb. The next stage of the simulation was devoted to the study of the response of the model to two kinds of boundary conditions varying with respect to time. The monthly averaged climatological wind-stress data were averaged to the seasonal ones and the linear interpolation was made between them. At first, a 3-year spin-up was carried out on the basis of the climatological data (Experiment IIIa). The quasi-flux conditions calculated on the basis of the Levitus data were set up for temperature and salinity on the surface. Then satellite seasonal wind-stresses were used for the wind forcing. The calculations were continued for the 2.5-year period (Experiment IIIb).

Results of simulation for Experiments IIIa and IIIb are presented in Figures 8–12. The integral stream function as in diagnostic Experiments Ia,b and IIa,b has qualitatively the same structure. However as it was mentioned above, the differences in the wind-stress amplitude lead to essential deviations in the values of the mass transport in some zones. In Figure 8, the deviations of mass transport values calculated with the use of the satellite data after the 2-year cycle from the initial diagnostic values are presented.

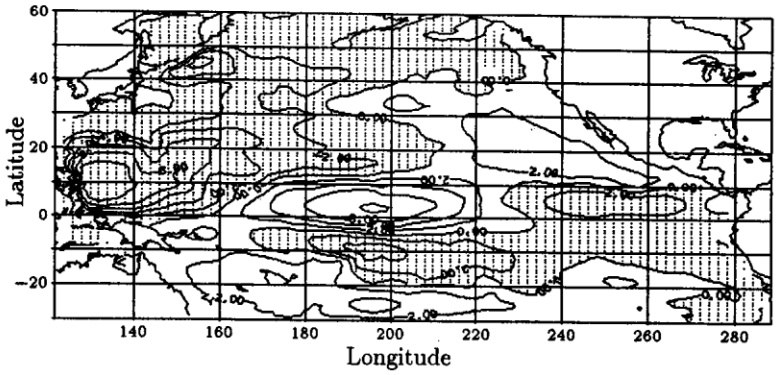

Figure 8. Integral stream function anomalies. The results of simulation for two year period with *Halpern* wind stress minus initial climatic state for winter

The amplitudes of the deviations reach 6 Sv in the central equatorial zone, 8 Sv in the eastern tropical zone and 6 Sv in the Oyashio region. The behaviour of these anomalies with respect to time is presented in the Hovmoller diagrams in Figures 9a, 9b, and 9c. These pictures give the time-longitude distributions of the integral stream function anomalies at latitudes 0, 10, and 35° N, respectively. In each zone, the time dependence of the anomalies have a distinct seasonal character. In the central part of the equatorial zone the anomalies move from east to west with the speed about two thousand km per month. This process is probably connected with changing the centers of the atmospheric forcing in a seasonal cycle. On the contrary, at latitudes 10 and 35° N the situation is different. The direction of the anomalies movement is reverse and is directed to the west. At latitude 10° N, the deviations in the western part of the basin are negative, whereas the central part, on the contrary, has a positive sign of the deviations.

At latitude 35° N, the satellite wind-stress data caused seasonal variations of mass transport, which are mainly positive and have a distinct negative inclination of isolines which testifies the anomalies shift to the east.

In connection with this, the following question arises: whether this distribution of the seasonal mass transport anomalies is typical of climatic seasonal variations as for a concrete period of 1994 or not? The answer to this question is given in Figures 10a and 10b. These are two diagrams similar to Figures 9a and 9c, but presenting the mass transport obtained in Experiment IIIb minus mass transport of Experiment IIIa in the seasonal cycle for the 2.5-year period. The pictures show that for the equatorial zone, the anomaly shift processes in climatic and satellite data experiments are identical, because the isolines are parallel to the abscissa axis. A distinct difference in the amplitude can be seen in the western part of the Pacific in the summer period. The reason is that for this period there is an essential

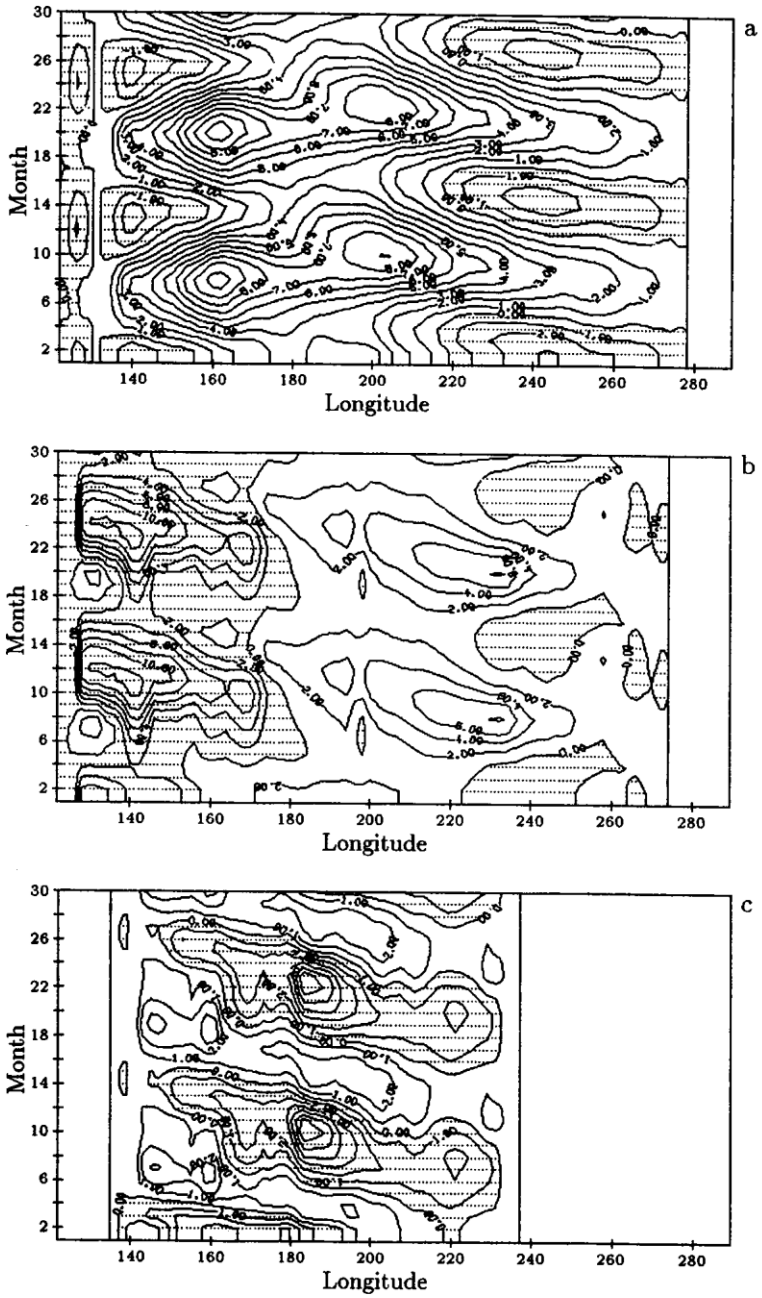

Figure 9. Hovmoller's diagram for integral stream function anomalies. Results of simulation for two and a half year period with *Halpern's* wind stress minus initial climatic state: (a) Equator; (b) latitute 10 N; (c) latitude 35 N

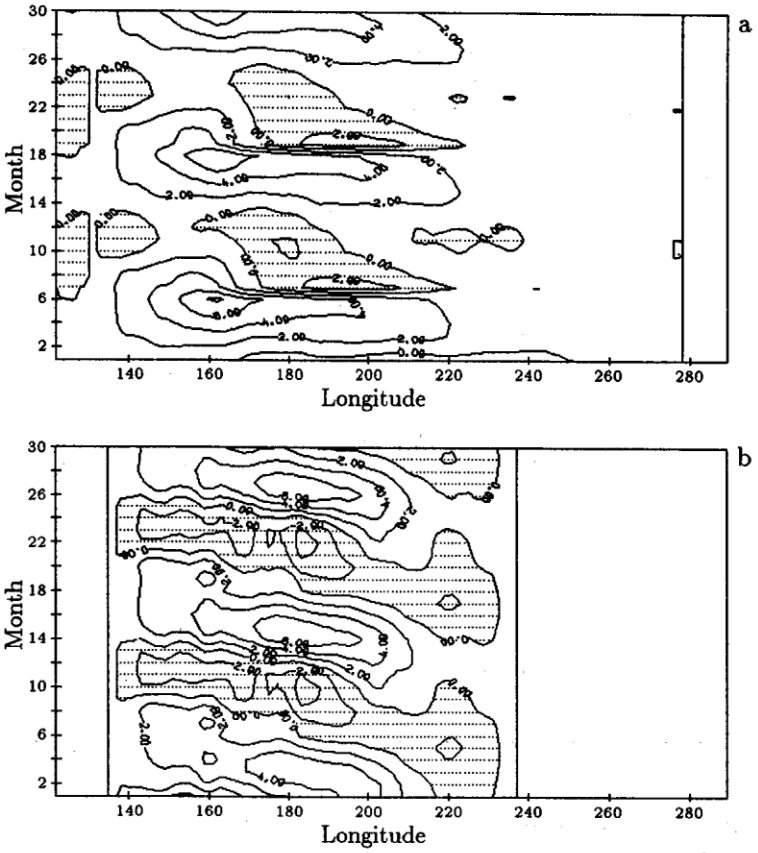

Figure 10. Hovmoller's diagram for integral stream function anomalies. Results of simulation for two and a half year period with *Halpern's* wind stress minus results with *Hellerman* wind stress: (a) Equator; (b) latitute 35 N

sharping of the wind-stress curl in the equatorial region in the climatic data. In 1994, the atmospheric circulation for this period in the equatorial region is much weaker. At latitude 10° N, the situation is similar.

In contrast to this, at latitude 35° N (Figure 10b) in the diagram there is also observed a negative inclination of the isolines. This means that the shift of the anomalies to the west in the climatic cycle is slower than in the 1994 year situation.

Let us come to the discussion of the 3-D velocity fields. In Figures 11a and 11b, the cross-sections of the zonal velocity at longitude 179° E after 1-year integration of Experiments IIIa and IIIb is presented. In Figure 11a, a zonal velocity component for the winter season in Experiment IIIa is plotted. The main specific features are observed in the equatorial zone. There is a westward jet near the surface which reaches a depth of 100 m. Below 150 m,

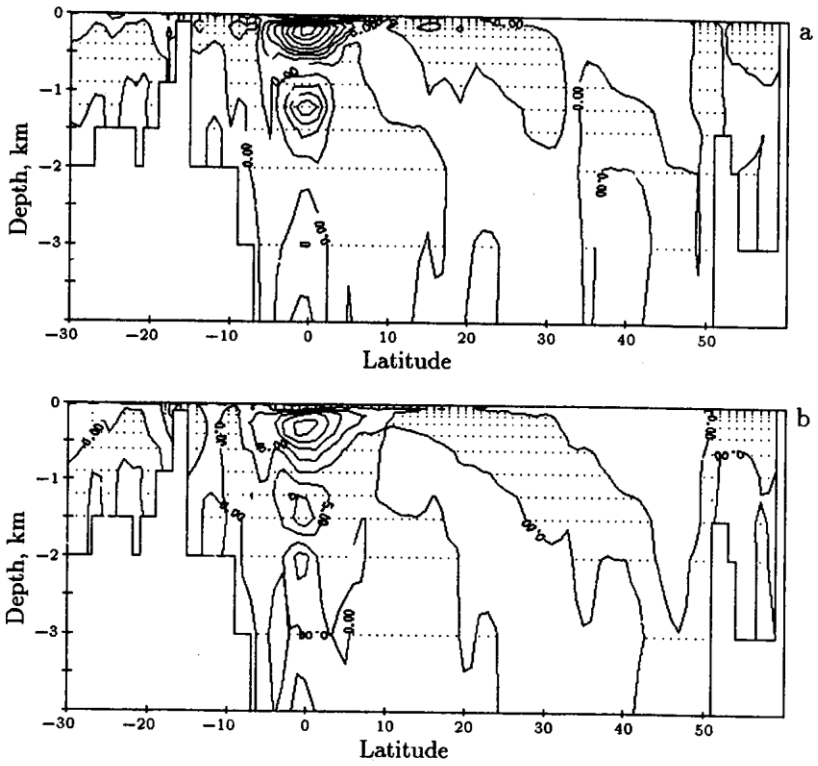

Figure 11. Cross section of the calculated currents – U-component. Results of simulation for 13 months with (a) *Hellerman* and (b) *Halpern* wind stress

there is an undercurrent which was formed during the prognostic calculation with a climatic seasonal cycle. The center of this jet is located at a depth of 300 m which is in agreement with observations. However, the value of the undercurrent is not as strong as in nature and reaches only 25 cm/s. This is typical of numerical models with coarse grids. Below the undercurrent at a depth of about 1000 m one more less intensive stream exists which is directed to the west.

Figure 11b presents the same characteristic for numerical experiment IIIb with satellite wind-stress for 1994. The main features are identical, but the intensity of the equatorial jets are somewhat weaker, which is connected with the less intensive wind-stress in this case. In the tropical, subtropical and subpolar zones, the main currents are concentrated near the surface and their signs correspond to the pictures of the horizontal velocity fields.

These distributions are presented in Figures 12a and 12b. Figure 12a shows the horizontal velocity field for Experiment IIIb after the 2-year period of integration at a depth of 100 m. One can see that there also exist the main Pacific ocean circulation gyres, but with the boundary currents weak enough.

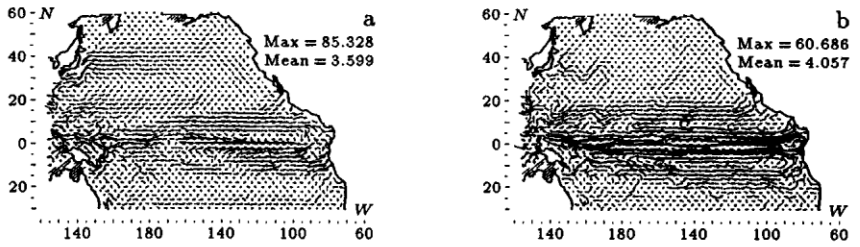

Figure 12. Current velocities at the depth $Z = 100$ m. Results of simulation for 13 months: (a) satellite; (b) satellite–climatic (anomaly)

The maximum velocity values reach the near equator area. Figure 12b shows the difference of the velocity field at a depth of 100 m between Experiments IIIb and IIIa. The picture also testifies that the climatic data give a more intensive forcing for the currents than the satellite ones.

5. Conclusion

The study presented in the paper shows that many of the major features of the general North Pacific circulation have been revealed in the simulation with the help of the numerical model discussed here. A comparison of the results obtained with the use of the climatological data and the satellite data permits us to make the following conclusions:

1. Even a small difference between the climatic and satellite wind-stress data can bring about substantial differences in the simulated currents.

2. The use of satellite data has resulted in decreased values of the volume transport although the general circulation has retained its main structural features in all the experiments.

3. Vorticity of the horizontal circulation becomes more intensive with the use of satellite data.

4. Distinct changes have been observed in the diagnostic results in the vertical structure of the boundary currents depending on the data used (climatological or satellite); the new eddy formations have appeared in the regions with the intensive wind vorticity (satellite data).

5. Comparison of the integral stream function distribution in the prognostic experiments shows essential variability of the centers of circulation both for climatic and satellite surface forcing. Seasonal anomalies of the mass transport are caused by the atmospheric influence and move to the east or to the west according to the wind anomalies variation.

6. The 3-D velocity field obtained in prognostic experiments from the satellite data are much weaker with respect to the horizontal and the vertical directions in comparison with the climatological ones.

Thus, the use of the satellite data in numerical modelling has shown not only the positive results. Nevertheless, it is obvious that the appearance of this new source of data with high resolution in space and time opens the new possibilities for the research of the ocean circulation. The general ocean circulation can be investigated not only in terms of the climatic states, but one can study the interannual variability of the general circulation as well as a tendency of the current to change in a particular region.

Acknowledgements. The authors gratefully acknowledge David Halpern's helpful comments.

References

[1] Hellerman S., Rosenstein M. Normal monthly wind-stress over the World Ocean with error estimates // J. Phys. Oceanogr. – 1983. – Vol. 13. – P. 1093–1104.

[2] Halpern D., Zlotnicki V., Brown O., Freilich M., Wentz F. An atlas of monthly mean distribution of SSMI surface wind speed, AVHRR/2 sea surface temperature, AMI surface wind velocity, and TOPEX/POSEIDON sea surface height during 1994. – JPL Publ. 97-1. – Pasadena: Jet Propulsion Laboratory, 1997.

[3] Platov G.A. Modeling of interacted boundary layers of atmosphere and ocean in the Kuroshio region. – Novosibirsk, 1989. – (Preprint / AN USSR. Sib. Branch. Computing Center; 850) (in Russian).

[4] Liu W.T., Tang W., Atlas R. Sea surface temperature exhibited by an ocean general circulation model in response to wind forcing derived from satellite data // Remote Sensing of the Oceanic Environment / I.S.F. Jones, Y. Sugimori, R.W. Stewart eds. – Tokyo: Seibutsu Kenkyusha, 1993. – P. 350–355.

[5] Rienecker M.M., Atlas R.M., Schubert S.D., Willet C.S. A comparison of surface wind products over the North Pacific ocean // J. Geoph. Res. – 1996. – Vol. 101, P. 1011–1023.

[6] Kuzin V.I., Moiseev V.M. Model of the North Pacific circulation // Proc. of Computing Center SD RAS. – 1993. – Vol. 1. – P. 19–46 (in Russian).

[7] Kuzin V.I., Moiseev V.M. Diagnostic and adjustment current calculations in the North Pacific // Izvestia AN. Physics of Atmosphere and Ocean. – 1996. – Vol. 32, № 5. – P. 680–689.

[8] Kuzin V.I., Moiseev V.M., Martynov A.V. The response of the North Pacific circulation model to various surface boundary conditions // Proceedings of 7th annual PICES meeting, Fairbanks, USA, 1998.

[9] Marchuk G.I. Numerical Solution of the Problems of the Atmosphere and Ocean Dynamics. – Leningrad: Gidrometeoizdat, 1972 (in Russian).

[10] Kuzin V.I., The Finite Element Method in the Ocean Processes Modeling. – Novosibirsk: Computing Center, 1985 (in Russian).

[11] Levitus S. World Ocean Atlas 1994 / National Oceanographic Data Center. – Washington: Ocean Climate Laboratory, D.C., 1994.